Computer Methods and Programs in Biomedicine 267 (2025) 108805

Contents lists available at ScienceDirect

Computer Methods and Programs in Biomedicine

journal homepage: www.sciencedirect.com/journal/computer-methods-and-programs-in-biomedicine

Predicting physiological hip joint loads with inverse bone remodeling using clinically available QCT images

Sebastian Bachmann [a,*], Gianluca Iori [b,c], Kay Raum [d], Dieter H. Pahr [a], Alexander Synek [a]

[a] Institute of Lightweight Design and Structural Biomechanics, TU Wien, Gumpendorfer Straße 7, Vienna 1060, Austria
[b] Institute for Biomedical Engineering, ETH Zürich and University of Zürich, Gloriastrasse 35, Zürich 8092, Switzerland
[c] SESAME - Synchrotron-light for Experimental Science and Applications in the Middle East, Allan 19252, Jordan
[d] Center for Biomedicine, Charité-Universitätsmedizin Berlin, Corporate Member of Freie Universität Berlin, Humboldt-Universität zu Berlin, Berlin, Germany, Berlin 12203, Germany

ARTICLE INFO

Keywords:
Inverse remodeling
Bone adaptation, load estimation
Clinical feasibility
Physiological loading
loading history
Homogenized finite-element

ABSTRACT

Background and objective: Assessing joint-level loading conditions *in vivo* is challenging due to invasive measurement or complex computation. Inverse bone remodeling (IBR) offers a different approach by recovering the loading conditions directly from computed tomography (CT) images of the bone microstructure by finding the magnitudes to a set of load cases that load the bone optimally, i.e., maximally homogeneously. An efficient IBR method was recently proposed based on homogenized finite element (hFE) models. This study compared the hip joint load predictions of hFE-based IBR with clinically feasible CT scans to those obtained with the current gold standard, micro-FE-based IBR.

Methods: A set of 20 proximal femora was scanned *ex vivo*, both with a clinical quantitative CT (QCT) scanner (0.3 mm resolution) and an Xtreme CT II (XCT2) scanner (0.03 mm resolution). Finite element (FE) models with decreasing complexity were automatically created from those images. Micro-FE (μFE) models based on XCT2 images served as a baseline. hFE models based on the QCT images were created as clinically feasible models. Further intermediate models were created to trace sources of errors. IBR was applied to predict the optimal scaling factors of twelve unit load cases distributed over the femoral head.

Results: The predicted loads of the newly developed workflow for QCT images within IBR followed a trend seen previously with hFE models created from high-resolution images, such as XCT2. The peak load magnitudes of μFE and hFE-based IBR were well correlated (R^2=76.8 %), and the overall distribution of the loads was similar. However, an additional peak load calibration was required to obtain quantitative agreement (CCC=82.8 %).

Conclusions: A thorough comparison of μFE-based IBR and hFE-based IBR using QCT data was performed for the first time. A clinically feasible workflow, including a peak calibration, is presented, allowing for fast prediction of physiological peak hip joint loads.

1. Introduction

Knowing the physiological *in vivo* loading conditions at the joint level is crucial for many clinical questions. Safety factors for specific activities can be calculated if the physiological peak loads are known [1,2]. Disease onset [3] or progression [4] can be predicted if changes in the physiological loads can be measured. Knowing the physiological loading conditions also helps develop patient-specific implants [5]. Although the loading conditions give valuable information on a patient-specific level, the actual measurement of such loadings is invasive and, thus, is typically not performed in healthy individuals [6]. Consequently, other indirect methods must be used to estimate the loading conditions *in vivo*. A large variety of such methods exists for that purpose. For example, a commonly used method is musculoskeletal modeling, which requires detailed information about the bones and surrounding soft tissue, such as the attaching muscles. Patient-specific models are desirable, but obtaining the individualized information to construct them is challenging [7–9]. Therefore, models based on templates or databases in

* Corresponding author.
E-mail address: bachmann@ilsb.tuwien.ac.at (S. Bachmann).

https://doi.org/10.1016/j.cmpb.2025.108805
Received 31 January 2025; Received in revised form 7 April 2025; Accepted 23 April 2025
Available online 24 April 2025

combination with patient data that are easily accessible are used instead [10].

Another approach that can be applied individually and circumvents the hard-to-obtain information is focusing solely on the bones and their internal microstructure. Bones constantly adapt and respond to external mechanical stimuli to distribute these loads optimally throughout the structure [11]. Consequently, the load leaves an imprint in the microstructure after prolonged and repeated external loadings due to bone (re)modeling [12]. This information can be interpreted using inverse bone remodeling (IBR). Briefly, in IBR, it is assumed that during regular daily activity, i.e., the activity patterns are similar over a prolonged time, the external loads acting on the bone result in a homogeneous cumulative daily stimulus at the micro level, as the bone is in homeostasis, i.e., no functional adaptation occurs. The daily stimulus is discretized into several load cases, which are applied with a unit force one after the other to a finite-element (FE) model of the bone to reconstruct the loading conditions from the bone microstructure. These unit loads are subsequently scaled by IBR using an optimization function. The magnitude of the load cases is then found by the optimization function, which scales the unit load cases to obtain a maximally homogeneous stimulus distribution. Several variations of the method have been developed over the past years regarding the FE model type and the optimization function. The FE model type ranged from 2D homogenized FE (hFE) models [13,14], over micro-FE (μFE) [15–17], to 3D hFE models [18–20]. The target stimulus in the optimization function is typically based on strain energy density (SED) or derived quantities such as effective strain.

This pool of existing methods allows one to choose a tailored approach for different questions. For example, if high-resolution CT data is available, one might use a μFE-based approach to get the best prediction. However, for clinical studies, such high-resolution images are rarely available. Thus, hFE-based approaches have to be used. As recently shown, such models offer comparable results with the additional benefit of extremely fast predictions compared to μFE models [18,19]. Even though the hFE workflow can be performed on clinical CT images [21–23], hFE-based IBR has so far only been tested using high-resolution images (<100 μm voxel size) rather than clinical CT images [18,19]. The usage of clinical CT images adds the following impediments over high-resolution CT images: (1) bone volume fraction (BV/TV) is not directly available, and only bone mineral density (BMD) can reliably be measured using a quantitative CT (QCT) scanner, where an additional calibration phantom in the scan is used to reconstruct the BMD from the Hounsfield-units. (2) the image resolution is coarser than previously used for IBR, typically in the range of a few hundred micrometers up to millimeters rather than tens of micrometers. (3) Consequently, the cortical bone is not represented by a sharp boundary in the image, and separating the cortical volume is more complicated.

Thus, the aim of this study was twofold: (1) to establish a workflow for IBR predictions based on clinically feasible QCT data of human proximal femora and (2) to use this workflow and compare the predicted hFE-based hip joint loads to the current gold standard, which is μFE-based IBR on high-resolution CT data, and *in vivo* peak hip joint loads measured with instrumented prostheses. Additional "intermediate" models with step-wise decreased levels of detail were created and compared to trace the error introduced by the models built upon QCT scans.

2. Methods

The overall workflow is shown in Fig. 1. The individual steps are described in detail below.

2.1. Image acquisition and processing

A set of 20 images of fresh frozen, cadaveric human proximal femora was acquired from a previous study [24], for which both QCT and high-resolution scans were available. All subjects had given consent for the scientific use of their bodies. Samples were collected for a previous study [24] at the anatomy institute of the Lübeck University in accordance with the German law ("Gesetz über das Leichen-, Bestattungs- und Friedhofswesen des Landes Schleswig-Holstein - Abschnitt II, §9 (Leichenöffnung, anatomisch)" from 04.02.2005). No additional scans or experiments were conducted on the specimens for this study. Detailed information on the samples (sex, age, side) is given in the supplemental material. Soft tissues were removed before scanning. For details on the sample preparation protocol, refer to Iori *et al.* [24] and Dall'Ara *et al.* [25].

The proximal femora were scanned *ex vivo* with a clinical QCT scanner (Siemens Somatom 64, Siemens AG Erlangen, Germany) using 120 kVp, 360 mAs, and a voxel size of 0.293 mm × 0.293 mm × 0.304 mm, using an established protocol [26–28], also possible *in vivo* [29]. A calibration phantom was included in each scan (QRM Model 3 CT Calibration Phantom #2337, QRM GmbH, Möhrendorf, Germany).

High-resolution scans were performed using an XtremeCT II (Scanco Medical AG, Brüttisellen, Switzerland), hereafter named XCT2, using 68 kVp, 1470 μA, and 200 ms integration time with a voxel size of 0.03 mm × 0.03 mm × 0.03 mm.

All XCT2 images were resampled to a voxel size of 0.09 mm × 0.09 mm × 0.09 mm to reduce noise in the images [16] and the computational costs of μFE without compromising the results of IBR [30]. All images were aligned to the "implant coordinate system" of the OrthoLoad data (refer to Fig. 1 in Bergmann *et al.* [6]) to allow subsequent

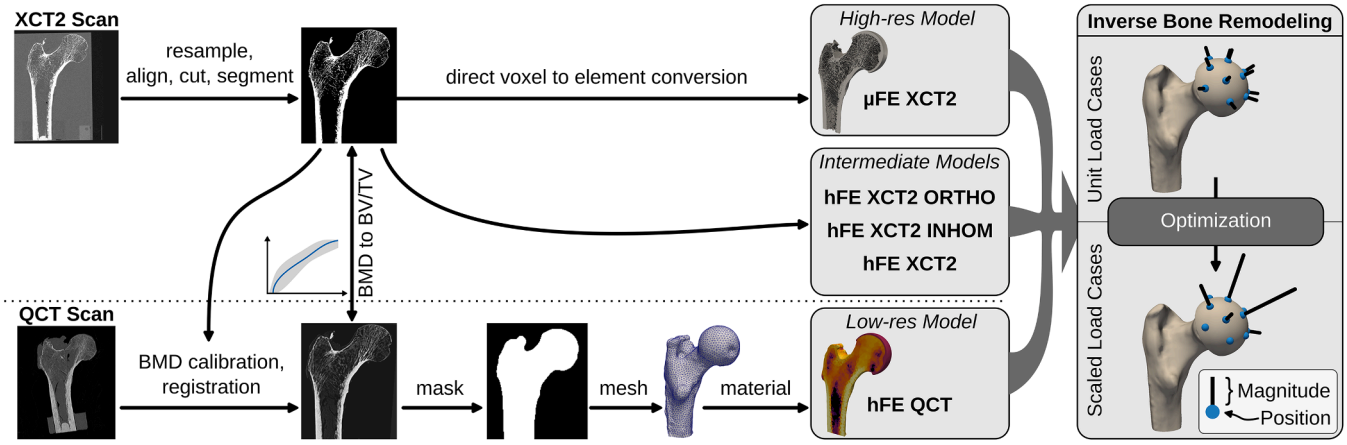

Fig. 1. Graphical overview of the study. Image processing workflow from CT image to FE model for XCT2 and QCT images. Additional intermediate models were created from the high-resolution images. Finally, inverse bone remodeling (IBR) is applied to the models to get scaling factors for a set of unit load cases.

comparisons and were cut at the shaft to uniform length. The cut-off length was specified to be $3R_{head}$ + 60mm, measured from the most superior part of the head (Fig. 2). The images were segmented using an individual threshold, calculated by asserting the same bone volume fraction (BV/TV) in the head region as for 0.06 mm images used in previous studies [16,19]. Labeled masks, separating the trabecular, cortical bone volume, and the background, were created as in a previous study [19].

The QCT images were rigidly registered to the aligned XCT2 images using "negative normalized cross-correlation" as a metric using SimpleITK 2.3.1 [31]. This ensured the same size and position as the XCT2 images. All QCT images were then individually calibrated from Hounsfield units (HU) for bone mineral density (BMD) using the calibration phantoms included in the scans using the protocol described by Dall'Ara *et al.* [32]. The images were resampled to an isotropic voxel size of 0.3 mm using linear interpolation for easier processing. Masks separating the bone volume from the background were created for the QCT images using the "fill" method [33].

2.2. Finite element modeling

As a baseline, μFE models were created in a direct voxel-to-element conversion [16,19], where each voxel is transformed into a 1st-order hexahedral element. A voxelized cartilage layer was added around the femoral head to aid the load transfer on the voxelized surface [16,19]. The dimensions of the cartilage layer were determined by the head size and are shown in Fig. 2.

Homogenized finite element (hFE) models were created from QCT data using a custom CGAL 5.5.1 [34] based mesh generator using 2nd-order tetrahedral elements. The characteristic mesh size was set to 3 mm, matching the size of elements used in a previous study but with a different mesh generator [19]. A cartilage layer was added using a custom gmsh [35] script [19], using 2nd-order tetrahedral elements with an upper limit of 1 mm element size. The surfaces of the bone and the cartilage layer were connected via a surface-to-surface tie constraint.

Boundary conditions were applied as described in previous studies [16,19]. Nodes at the cut surface at the distal part of the shaft were constrained in all three degrees of freedom. Unit load cases were applied in a circular area of 40 ° on the cartilage layer [16,19]. Nodal forces were applied in the case of μFE, while a distributed surface pressure with the same effective force magnitude was used in the case of hFE models [19].

Models with different levels of detail and meshing strategy ("intermediate models") were created additionally to the μFE and hFE models described above. These intermediate models were used to determine sources of errors due to different hFE material modeling and mesh generation strategies. Furthermore, they allowed for the comparison of the results to previous studies.

Two models using a separate cortical volume were created, as described in a previous study [19]. However, large models, including the shaft, were created instead of using only the head region. These models use 2nd-order tetrahedral elements for the trabecular volume and 2nd-order wedge elements for the cortical volume. Both models used the same mesh but two different material models for the trabecular volume, namely an inhomogeneous orthotropic material (hereafter named "hFE XCT2 ORTHO") and an inhomogeneous isotropic material (hereafter named "hFE XCT2 INHOM"). An inhomogeneous isotropic material was used for the cortical volume in both cases. Material properties were assigned as in a previous study [19]. A third hFE model (hereafter named "hFE XCT2") was created using a similar workflow as with the QCT images, i.e., without a separate cortical volume. However, the inhomogeneous isotropic material was assigned using BV/TV calculated directly from the XCT2 images.

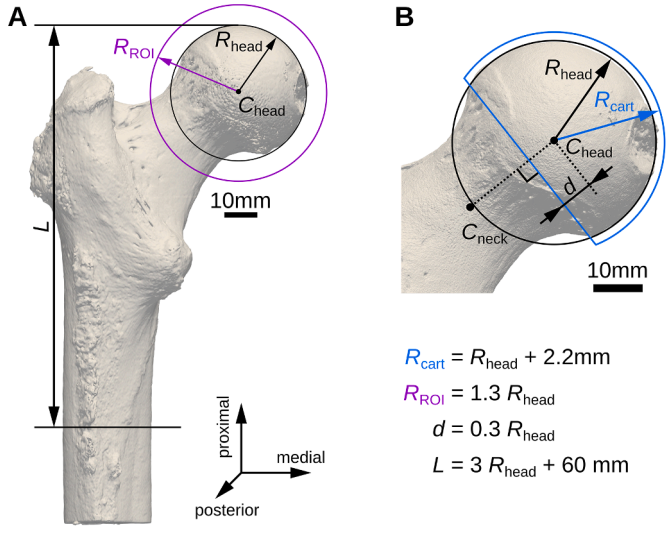

Fig. 2. (A) Cut-off length of the femur and size of the ROI used in IBR and (B) construction of the cartilage layer.

2.3. BV/TV calibration

For the material mapping of the finite element models and hFE-based IBR in general, the bone volume fraction (BV/TV) ρ is required. BV/TV can be calculated using voxel counting for the segmented XCT2 images, but the calculation is not straightforward for the BMD-calibrated QCT images. Several calibration models are available in the literature to calculate ρ from BMD, for example, using a linear relationship [32] or higher-degree polynomials [36]. To ensure direct comparability between XCT2 and QCT images, a BMD-BV/TV relationship was fitted on the pooled BMD and BV/TV values of all elements of the hFE QCT and hFE XCT2 models using polynomials [36]. The BMD value from QCT and BV/TV value from XCT2 images were mapped onto the same mesh for each bone using a background grid method [37], the same method for material mapping later on. In both cases, the VOI diameter was set to $D_{VOI} = 3.5$ mm, and the grid distance to $\delta_{grid} = 1.6$ mm. Then, the value for each mesh-element was collected for each bone and polynomial functions with increasing degree were fitted on the full dataset. The constant in each function was enforced to be zero to ensure zero BV/TV for zero BMD. The residuals were calculated and F-tests were used to compare the variances of the residuals to the ones of the previous fit [36]. The model with the highest degree was used, where still a significant change ($p < 0.05$) to the previous polynomial function was observed.

2.4. Material law

All material properties are summarized in Table 1. The μFE models used a homogeneous isotropic material for bone with $E = 12{,}000$MPa and a Poisson's ratio $\nu = 0.3$ [18,19,38]. The hFE models created from QCT images used an inhomogeneous isotropic material for bone using a

Table 1
Material properties for all used FE models. tb: Trabecular volume. ctx: Cortical volume.

Model	E_0 (MPa)	ν_0 (-)	G_0 (MPa)	k (-)	l (-)	δ_{grid} (mm)	D_{VOI} (mm)
μFE XCT2	12,000↑	0.3	-	-	-	-	-
hFE ORTHO - tb	13,758↑	0.22	4136	2.01	1.2	2.5	5.0
hFE ORTHO - ctx	12,000↑	0.3	-	2.0	-	2.5	5.0
hFE INHOM - tb	10,905↑	0.2526	-	2.0	-	2.5	5.0
hFE INHOM - ctx	12,000↑	0.3	-	2.0	-	2.5	5.0
hFE XCT2	10,905↑	0.2526	-	2.0	-	1.6	3.5
hFE QCT	10,905↑	0.2526	-	2.0	-	1.6	3.5
Cartilage	10↑	0.3	-	-	-	-	-

density-dependent power law for the elastic modulus: $E = E_0\rho^k$. Material properties were taken from literature and matched the homogenous material for the μFE models [39]. The material parameters were $E_0 = 10,905$MPa, $\nu = 0.2526$, $k = 2.0$. The material was mapped using a background grid [37] with distance $\delta_{grid} = 1.6$ mm and a spherical VOI with diameter of $D_{VOI} = 3.5$ mm. The VOI size was smaller than previously used ($D_{VOI} = 5$ mm and $\delta_{grid} = 2.5$ mm) as a smaller VOI results in a sharper gradient of the density [40,41]. A smaller VOI can be applied if no orientation, i.e., anisotropy, is used in the material model, as long as the continuum assumption applies [42], and the voxel size is smaller than the VOI size. The bone material and mapping parameters of the intermediate hFE models (hFE ORTHO, hFE INHOM, and hFE XCT2) were consistent with a previous study [19]. Briefly, hFE ORTHO uses a Zysset-Curnier-type inhomogeneous, orthotropic material [43] for trabecular bone with $E_0 = 13,758$MPa, $G_0 = 4136$MPa, $\nu_0 = 0.22$, $k = 2.01$, $l = 1.2$ and a power-law-type inhomogeneous material for cortical bone with $E_0 = 12,000$MPa, $\nu = 0.3$, $k = 2.0$. hFE INHOM and hFE XCT2 use the same material properties for trabecular bone as hFE QCT. The cortical bone model for hFE INHOM was the same as for hFE ORTHO.

The cartilage layer was assigned a homogeneous isotropic linear elastic material with $E = 10$MPa and $\nu = 0.3$ for both μFE and hFE analysis [16,19], as the μFE solver ParOSol only supports a single Poisson's ratio for the whole mesh [44]. Thus, this simplified cartilage material was kept in the homogenized models for comparability.

2.5. Inverse bone remodelling

Details on the inverse bone remodeling (IBR) method can be found in Christen *et al.* [15] for a pure μFE approach and Bachmann *et al.* [18] for an adaptation to homogenized FE models. In brief, the cumulative daily mechanical stimulus acting on the bone is discretized into a set of unit load cases, L_i (Fig. 3), acting for an equal amount of time. The magnitude of these discretized loads can be found by applying each unit load case subsequently to an FE model of a bone. The strain energy density (SED) $U_{j,i}$ for each element or integration point j is collected for each of the load cases i and used in an optimization procedure to find scaling factors α_i for the load cases that load the bone in an optimal (i.e., homogeneous) way, according to remodelling theory. A tissue target stimulus $\widetilde{U}_0$ is used to define the target value in the optimization function. In a recent adaptation of IBR for hFE, an additional density exponent d is used to relate the SED at the continuum level to an equivalent SED at the micro-level using the BV/TV ρ_j of each element [18]. Rather than using the load scaling factors α_i in the optimization function directly, they are replaced by a scaling factor for the SED $s_i = \alpha_i^2 N_i/N_{tot}$ instead. Each unit load case is applied N_i times per day (load cycles) and N_{tot} is the total number of load cycles for all unit load cases. Here, N_i is set to 1, as it is assumed that all unit load cases act an equal amount per day [45], and thus $N_{tot} = N_{LC}$, the total number of unit load cases. The applied optimization function can then be written as the minimization of the residual function $r(s_i)$:

$$\min_{s_i \in \mathbb{R}_0^+} r(s_i) = \sum_{j=1}^{N_{IP}} \left(\widetilde{U}_0 \, \rho_j^d - \sum_{i=1}^{N_{LC}} s_i \, U_{j,i} \right)^2 V_j \tag{1}$$

where N_{IP} is the total number of integration points and V_j is the volume of each integration point.

A total of $N_{LC} = 12$unit load cases were used to discretize the daily stimulus: Four unit load cases in the frontal plane, as described in the literature [16,19], and additional four unit load cases anteriorly and posteriorly were applied onto each bone. The unit load cases were modeled using a 40 ° cone, with the tip at the center of the head and a resultant force magnitude of $F_{unit} = 1$kN [16,19]. The optimization was then performed using all twelve load cases, and the predicted force magnitude of each load case was computed as $F_i = \alpha_i F_{unit}$. Fig. 3 shows the applied load cases in a 2D projection and the local coordinate system at the proximal femur, which matches the "implant coordinate system" from Bergman *et al.* [6].

The IBR optimization function for homogenized FE models was used [18]. The density exponent was set to $d = 1.297$, according to a previous parameter identification [19]. The target stimulus was set to $\widetilde{U}_0 = 0.02$ MPa as reported in literature [15,16,18,19]. Only the elements inside a sphere of radius $1.3R_{head}$ around the femoral head center were used for the optimization [19].

2.6. Calibration of peak loads

Previous studies showed that hFE-based IBR can capture the overall distribution of load cases, but the predicted magnitudes may differ in comparison to μFE-based IBR [18,19]. An additional calibration to a known load can ensure comparable magnitudes of the predicted loads without affecting the load distribution. Such a calibration law has to be established only once per model type (i.e., μFE XCT2 or hFE QCT), ideally using a representative cohort of samples. Afterwards, it can be applied to new individuals without further ado, if the same model type is used.

In addition to the unmodified IBR prediction, the predicted load

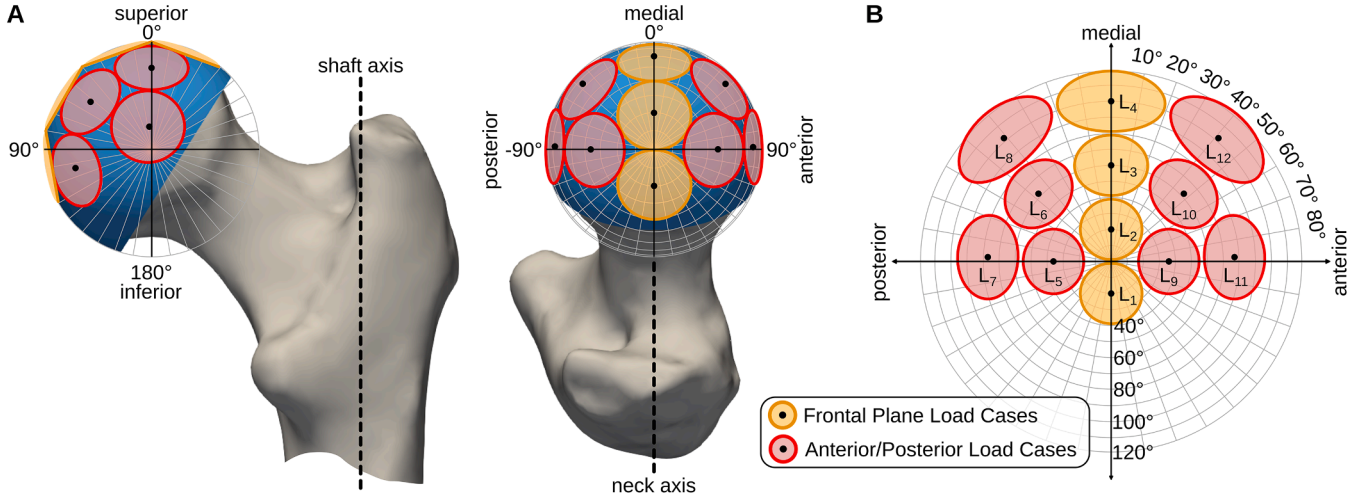

Fig. 3. Definition of coordinate system and unit load cases. (A) Alignment of the bone and 3D overview of the load cases. The superior-inferior axis is parallel to the shaft axis. The medial-lateral axis is parallel to the neck axis. The unit loads are added in spherical regions of 40 ° diameter onto the sphere. (B) Projection of the spherical coordinate system into a 2D polar plot, including the load case numbers L_1 to L_{12}.

cases were scaled by an adjustment factor κ_p that is specific to each model variant. It is found by relating the average predicted peak load of all samples to a known load of level p. For this study, a reference level κ_{2700} (i.e., $p = 2.7$kN) was used, as it resembles approximately the average patient-specific peak hip joint force for the "daily activities" (walking, stairs up, stairs down, stand up, sit down, and stance) [16] measured with the OrthoLoad hip-implant system [6].

For each of the tested FE methods, the peak forces are gathered from all n models, and the adjustment factors are calculated for each method using ordinary least squares as

$$\kappa_p = p \, \frac{\sum_{i=1}^{n} F_{\text{peak},i}}{\sum_{i=1}^{n} F_{\text{peak},i}^2} \tag{2}$$

Afterward, the resulting vector of scaling factors predicted by IBR is multiplied by the method-specific adjustment factor to get the calibrated scaling factors $\widehat{\alpha}_i = \kappa_p \alpha_i$ and consequently $\widehat{F}_i = \widehat{\alpha}_i \, F_{\text{unit}}$.

2.7. Software and hardware

Image processing was performed in medtool 4.7 (Dr. Pahr Ingenieurs e.U., Pfaffstätten, Austria, http://www.medtool.at) and SimpleITK 2.3.1 [31]. All μFE models were solved with ParOSol [44], and the homogenized models were solved with ABAQUS V6R2024 (Dassault Systèmes, Vélizy-Villacoublay, France). Pre- and post-processing was done using Python 3.9.7 (Python Software Foundation, https://www.python.org). The inverse bone remodeling algorithm was implemented using scipy 1.10.0 [46].

All homogenized models were solved on a dual AMD EPYC 7763 server, using 4 CPU cores. The μFE models were solved on a cluster of servers with different hardware configurations, ranging from 52 to 66 CPUs in parallel.

3. Results

3.1. BMD to BV/TV relation

A total of 588,885 elements from the 20 samples were used to fit the polynomial function for BMD and BV/TV. The lowest degree polynomial after which no significant decrease in the variance of the residuals was observed was of degree 6:

$$\begin{aligned}\rho(x) = {} & 1.6 \times 10^{-3} x + 9.9 \times 10^{-7} x^2 - 9.3 \times 10^{-9} x^3 \\ & + 1.7 \times 10^{-11} x^4 - 1.2 \times 10^{-14} x^5 + 3.2 \times 10^{-18} x^6\end{aligned} \tag{3}$$

With x being the BMD of the QCT image. The BV/TV was clipped to the interval [0, 1] after the calculation from BMD. Fig. 4 shows the fitted polynomial, including the clipping for higher values than 1 or lower than 0.

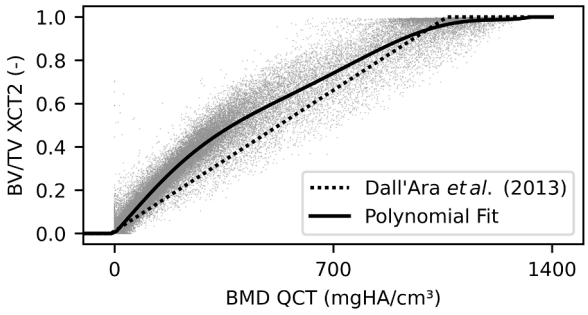

Fig. 4. Plot of polynomial fit over the gathered data and comparison to linear calibration law given by Dall'Ara *et al.* [32]. Only a subsample of 10 % of all points is shown to highlight the overall distribution.

3.2. FE model runtimes

The μFE models contained between 66,945,796 and 115,910,667 elements (mean 91,121,390), and the hFE models contained between 66,273 and 107,733 elements (mean 85,023), both including the cartilage layer. The number of nodes varied between 88,235,799 and 150,322,570 (mean 117,322,878) for μFE and 118,118 and 184,596 (mean 147,105) for hFE.

The mean runtime (wall clock) for the hFE models was 54.9 s (standard deviation 9.4 s) using 4 CPUs. The μFE models were solved on different servers with different hardware configurations. Thus, no standardized runtime can be given. The average runtime (wall clock) was 40 h (standard deviation 23.8 h).

3.3. Intermediate model results

The resulting scaled loads (without calibration for peak load) for the μFE XCT2 and hFE QCT models and additional intermediate models are shown in Fig. 5. A detailed plot containing all individual samples is given in the supplemental material. Different patterns can be observed for the hFE models. Most prominent is the overall decrease for F_2 and F_{10}, which follows almost a monotonic trend from μFE XCT2 towards hFE QCT. Conversely, F_3 and F_8 gets larger for all hFE models compared to μFE, but decreases until reaching almost the same value as μFE with the hFE QCT model. Similarly, F_1,F_6, F_9, and F_{12} are lower for the hFE models and increase in hFE QCT to almost the same level as in μFE XCT2. The other load cases do not show a distinct pattern (F_4) or are close to zero (F_5,F_7, F_{11}). All samples show a similar pattern with only a few outliers (plot in supplemental material).

3.4. Predicted hip joint loads

The resulting peak-calibration factors κ_{2700} for a reference peak load of 2.7kN were 0.514 and 0.685 for μFE XCT2 and hFE QCT, respectively. Fig. 6 shows the predicted load cases for the frontal plane as a subset of all load cases before and after peak calibration. The peak load was predicted as F_2 and $\widehat{F}_2$ in all models. The pattern of load cases after the peak calibration shows that $\widehat{F}_2$ and $\widehat{F}_4$ are similar but $\widehat{F}_3$ is overestimated and $\widehat{F}_1$ is underestimated in hFE QCT.

The distribution of scaled loads as a projection from the sphere is shown in Fig. 7 and the numerical values are given in Table 2. In general, there was a tendency for load cases to be smaller in hFE than in μFE, with the exception of $\widehat{F}_3$, which is on average 36 % larger in hFE. Next to the peak $\widehat{F}_2$, two load cases ($\widehat{F}_9$ and $\widehat{F}_{10}$) scaled highest on the anterior side, as well as one load case ($\widehat{F}_6$) on the posterior side and one in the frontal plane ($\widehat{F}_3$). All other load cases were scaled below 1kN, with mean values less than 0.5kN. The absolute difference between μFE XCT and hFE QCT was, on average, 0.1kN. The largest differences were found for $\widehat{F}_1$, $\widehat{F}_3$, $\widehat{F}_{10}$, and $\widehat{F}_{12}$ with absolute differences of up to 0.31kN.

Correlation plots of μFE XCT2 and hFE QCT are shown in Fig. 8, and the coefficient of correlation (R^2) and concordance correlation coefficient (CCC) are given in Table 2. The highest correlations were found for the peak loads. Low correlation was found for load cases farthest away from the peak, as these were often zero in μFE XCT2 but have a small non-zero value in hFE QCT.

4. Discussion

The aim of this study was to compare predictions of inverse bone remodeling based on clinically feasible QCT images with the current gold-standard, μFE-based IBR using high-resolution CT images. The study provides evidence that QCT images with a ten times lower resolution than XCT2 can be used to predict peak hip joint loading using a slightly modified IBR workflow, which takes into account the specifics of

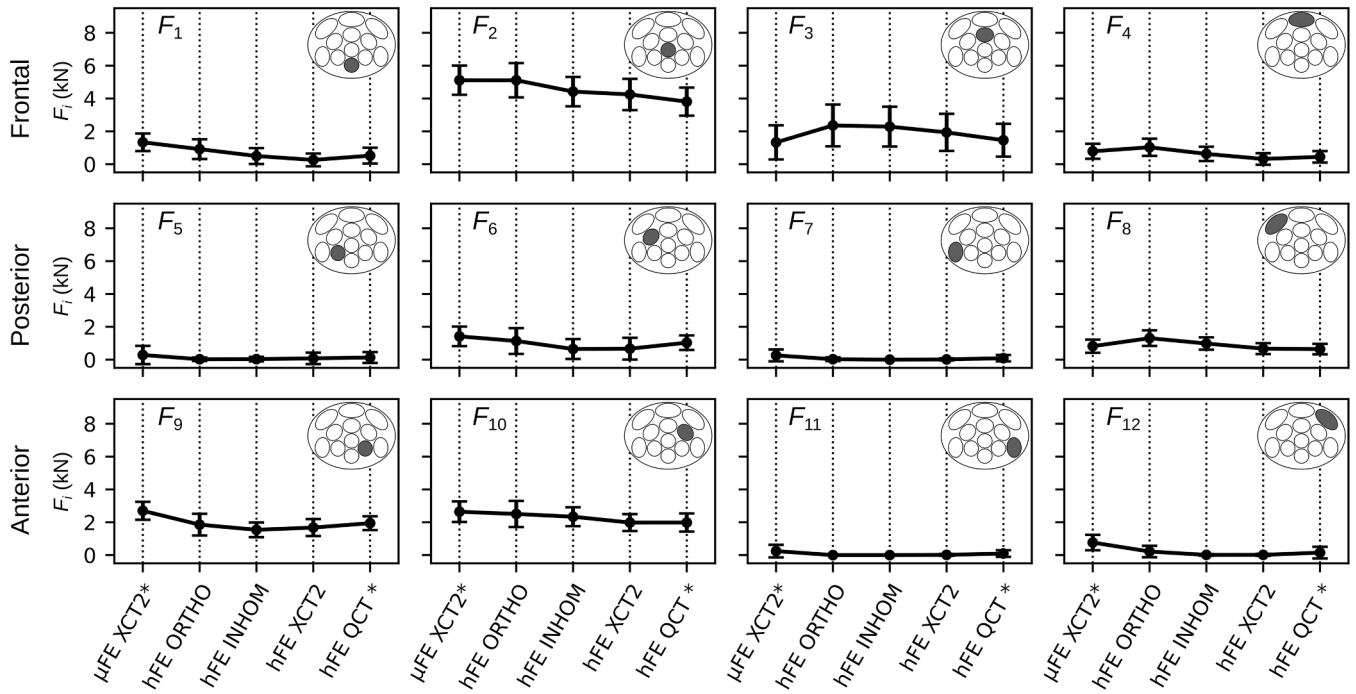

Fig. 5. Progression of load scaling factors (without calibration for peak load) for all models, including intermediate models. Shown is mean ± standard deviation for all samples ($n = 20$). Models marked with an asterisk (*) are the gold standard models (μFE XCT2) and the clinically feasible models (hFE QCT).

QCT images. The overall distribution of predicted load cases was similar between XCT2 and QCT-based IBR. However, the magnitude of the prediction of QCT-based IBR was lower on average than those of μFE-based IBR, and the μFE-based IBR prediction was higher than the measured *in vivo* peak forces during daily activities measured with instrumented prostheses. Calibrating the models for the peak load, based on measured *in vivo* peak forces, resulted in a good qualitative agreement in the overall distribution of the loads and a high correlation of the peak loads between μFE and hFE-based IBR.

The new workflow for using QCT images within IBR required only minor modifications compared to the previously developed workflow for high resolution CT images. The main differences were the required BMD to BV/TV calibration and optional minor adjustments in the material mapping. The change in predicted loads followed a trend already observed with hFE-based IBR, i.e., lower predicted loads on average than with μFE-based IBR [19]. As previously suggested, it is possible to scale the predicted loads to a desired range [18]. Such a scaling was considered necessary for this dataset, as the hFE-based predicted peak loads deviated largely. It should be noted that this scaling, or peak calibration, does not affect the distribution of loads as all loads are scales with a constant factor.

A high correlation was found for the peak loads. However, load cases with lower predicted magnitudes showed only low correlations and a trend to be higher in hFE models than in μFE. Conversely, a general trend towards lower peak loads can be observed for all hFE model types (Fig. 5).

This behavior can partially be explained by a lower overall stiffness of the hFE models. This hypothesis was tested by additional evaluation of the displacement of the femoral head center for the different models. All hFE models showed a larger displacement than observed in μFE models, i.e., a softer model response, for all twelve load cases. Conversely, a higher stiffness of hFE QCT models compared to μFE was reported earlier [47]. However, these models used different material mapping and homogenized voxel-FE models instead of smooth meshes. The here applied material mapping has a smoothing effect on the elastic properties in the lower-resolution images, as the material properties are averaged over larger volumes during the material mapping. This behavior was also observed in a previous study [18]. Thus, regions with a locally low density in μFE may be assigned a slightly higher density in hFE. Hence, load cases applied in those regions can propagate loads into larger volumes of the hFE models, an effect that causes hFE-based IBR to increase the scaling factors for these loads.

Another explanation for this softer model response may be the increased volume of the hFE QCT meshes compared to hFE XCT2. The resulting mesh volume increased slightly as the cortical boundary is no longer depicted by a sharp edge in QCT images. Thus, the measured BV/TV in the cortical shell is lower, and the calculated Young's modulus decreases. Several methods were developed to circumvent these issues and may be applied in the future. For example, the cortical shell can be found by modeling the density profile of the CT image [48] or by increasing the stiffness of the cortical elements by using a "tissue function" [32,40].

The additional anterior and posterior load cases allowed for a better spatial prediction of the *in vivo* load, compared to previous studies where only loads in the frontal plane were used [16,19]. For example, the peak force during walking measured by OrthoLoad [6] is tilted by approximately 11 ° anteriorly in the sagittal plane and approximately 33 ° anteriorly in the transverse plane. Likewise, IBR predicts an anterior loading in a plausible location (i.e., $\widehat{F}_9$ and $\widehat{F}_{10}$) and a band of high load cases can be observed in the posterior-anterior direction ($\widehat{F}_6$, $\widehat{F}_2$, $\widehat{F}_3$, $\widehat{F}_9$, $\widehat{F}_{10}$), similarly to the contact pressure distribution at the hip joint [49].

The additional load cases introduce difficulties when comparing the model to the four load cases that were previously used [16,19] as the identified peak forces got higher. This behavior can be explained by the used optimization function (Eq. (1)). While the SED scaling factors s_i inside the optimization function got lower with more load cases, the load scaling factors $\alpha_i = \sqrt{s_i\, N_{\text{tot}}/N_i}$ for an increasing number of load cases $N_{\text{tot}} = N_{\text{LC}}$ got higher. For the here used approach, all loads are assumed to act an equal amount of time per day ($N_i = 1$) [45], and thus, all load cases contribute with the same amount to the cumulative stimulus, and consequently, the SED scaling factor at the peak load gets lower.

Two options are available to solve this issue. Either the number of loads per day N_i are known *a priori* for each load case and thus the loads

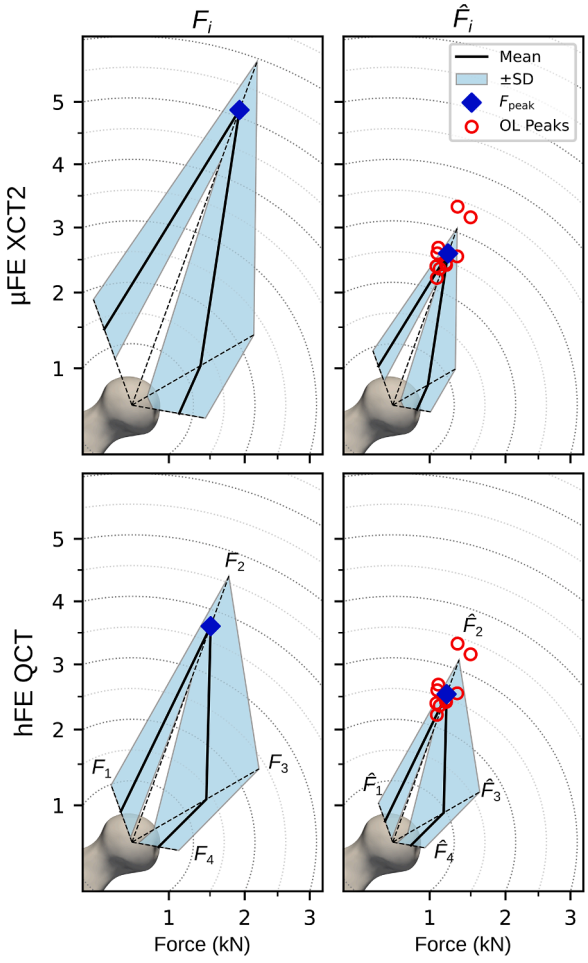

Fig. 6. Predicted loads in the frontal plane of the raw IBR prediction (left column) and the adjusted loads to a reference level κ_{2700} (right column). Shown are the peak loads measured with the OrthoLoad (OL) system [6].

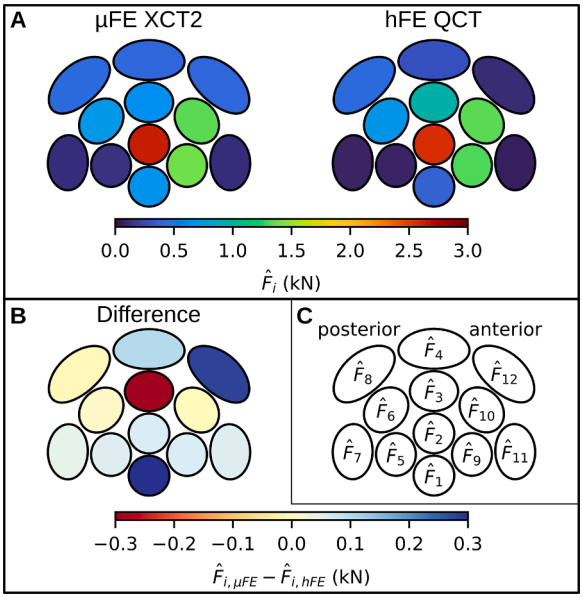

Fig. 7. (A) Distribution of the mean of scaled and peak-calibrated loads for all twelve load cases. (B) Mean of pair-wise differences between µFE XCT2 and hFE QCT. (C) Overview of load cases for reference.

can be individually scaled [15], or the resulting loads are calibrated in magnitude to a known value. Calibration for peak load was performed in this study. This type of calibration can be applied independently for each model type (i.e., µFE or hFE).

However, even with such a calibration, the number of unit load cases cannot be increased arbitrarily. Including known improbable loads may lead to situations where these loads contribute to the stimulus and artificially decrease other load cases. Similarly, the prediction degenerates when overlapping load cases are used [16]. Due to the high correlation of the resulting SED distributions to each other, the solution to the least-squares problem becomes ambiguous [50].

Thus, in the current form of the optimization function, only plausible load cases should be used, keeping implausible load cases to a minimum. With the current set of load cases, no unrealistic scaling of unphysiological loads (such as L_4 and L_8, which are close to the fovea capitis) was observed, which indicates that a small number of unrealistic loads may be acceptable as long as no correlated loads (i.e., overlapping) are added. If a set of plausible load cases cannot be defined *a priori*, another approach could be to either add a regularization function to the optimization to enforce physiological loads or scale the load cases independently from each other and avoid a dependency on the number of load cases or correlations.

The requirement for proper *a priori* load cases is an inherent limitation of the IBR method. Furthermore, it has to be assumed that the CT images were taken when the bone was in homeostasis, i.e., no adaptation of the bone was taking place at the time. Additionally, IBR cannot distinguish if an adaptation of the bone, visible in the CT image, is due to an actual mechanical signal, genetics, pathologies, or something else. It was shown for µFE-based IBR on trabecular bone cubes that the resulting SED distribution after the optimization was not perfectly homogeneous, highlighting that other factors than the pure mechanical stimulus affect the bone and are not captured by IBR [51].

The BMD to BV/TV polynomial used in this study yields higher values than the linear model from Dall'Ara *et al.* [32]. This discrepancy may be due to different CT scanners and image resolutions for the measurement of BV/TV. Here, a resampled resolution of 90 µm was used, based on XCT2 scans, while Dall'Ara *et al.* [32] had a resolution of 18 µm, imaged with a µCT. Furthermore, Dall'Ara *et al.* [32] used only a few regions in the femur for the comparison, while in this study, BV/TV and BMD were compared for each element.

Another study found a similar nonlinear relationship for BMD measured with HR-pQCT and BV/TV measured with µCT [36]. However, only a 4^{th}-degree polynomial instead of a 6^{th}-degree was required.

The BMD-BV/TV relationship may be simplified, as the curve follows a linear relationship until approximately 400 mgHA/cm^3. Thus, for example, a piecewise linear or polynomial function could be used.

The calibration was performed using the same method and parameters as in the subsequent material mapping, using a background-grid [37]. However, the choice of the parameters will influence the acquired calibration curve (see supplemental material): Both BMD and BV/TV are not sensitive to the choice of δ_{grid} as long as $\delta_{grid} \leq D_{VOI}/2$, but larger D_{VOI} tend to produce lower BMD and BV/TV, closer to the overall mean, as more and more voxels are averaged, while lower D_{VOI} resolve the local structure better. This means, that the here given calibration is only valid for these background-grid parameters and calibration has to be repeated if these parameters are changed.

Limitations of this study are the small sample size and relatively high age of the body donors, which are not representative of an entire population. The QCT images were created *ex vivo* with a voxel size of around 0.3 mm, while clinical routine scans typically use a lower resolution. Nevertheless, such high-resolution QCT scans are possible *in vivo*, not only with the applied QCT protocol [29] but especially with modern photon-counting detector CT (PCD-CT) [52,53] or by using deep-learning methods to enhance the resolution ("super-resolution") [54]. However, a high resolution may not be required for using hFE-based IBR. The material properties are computed from averages of

Table 2
Mean± standard deviation of predicted loads (peak-calibration reference level κ_{2700}), mean ± standard deviation of pair-wise differences, and coefficients of correlation and concordance correlation coefficient (CCC) for µFE XCT2 and hFE QCT.

	µFE XCT2 (kN)		**hFE QCT** (kN)		**Difference** (kN)		R^2 (%)	**CCC** (%)
$\widehat{F}_1$	0.68	± 0.271	0.36	± 0.321	0.3125	± 0.315	19.8	27.7
$\widehat{F}_2$	2.63	± 0.445	2.56	± 0.608	0.0653	± 0.306	76.8	82.8
$\widehat{F}_3$	0.66	± 0.528	0.96	± 0.695	−0.2955	± 0.384	70.1	72.0
$\widehat{F}_4$	0.40	± 0.228	0.30	± 0.235	0.0995	± 0.265	11.9	31.5
$\widehat{F}_5$	0.14	± 0.280	0.08	± 0.222	0.0540	± 0.115	84.9	87.6
$\widehat{F}_6$	0.72	± 0.302	0.70	± 0.295	0.0129	± 0.266	36.4	60.3
$\widehat{F}_7$	0.13	± 0.183	0.08	± 0.146	0.0491	± 0.215	2.5	14.8
$\widehat{F}_8$	0.42	± 0.203	0.42	± 0.227	−0.0064	± 0.178	43.7	65.7
$\widehat{F}_9$	1.38	± 0.273	1.32	± 0.286	0.0654	± 0.267	29.7	52.9
$\widehat{F}_{10}$	1.35	± 0.317	1.35	± 0.375	0.0020	± 0.359	22.4	46.7
$\widehat{F}_{11}$	0.12	± 0.194	0.06	± 0.135	0.0559	± 0.181	19.9	39.5
$\widehat{F}_{12}$	0.39	± 0.235	0.11	± 0.242	0.2811	± 0.238	25.3	29.1

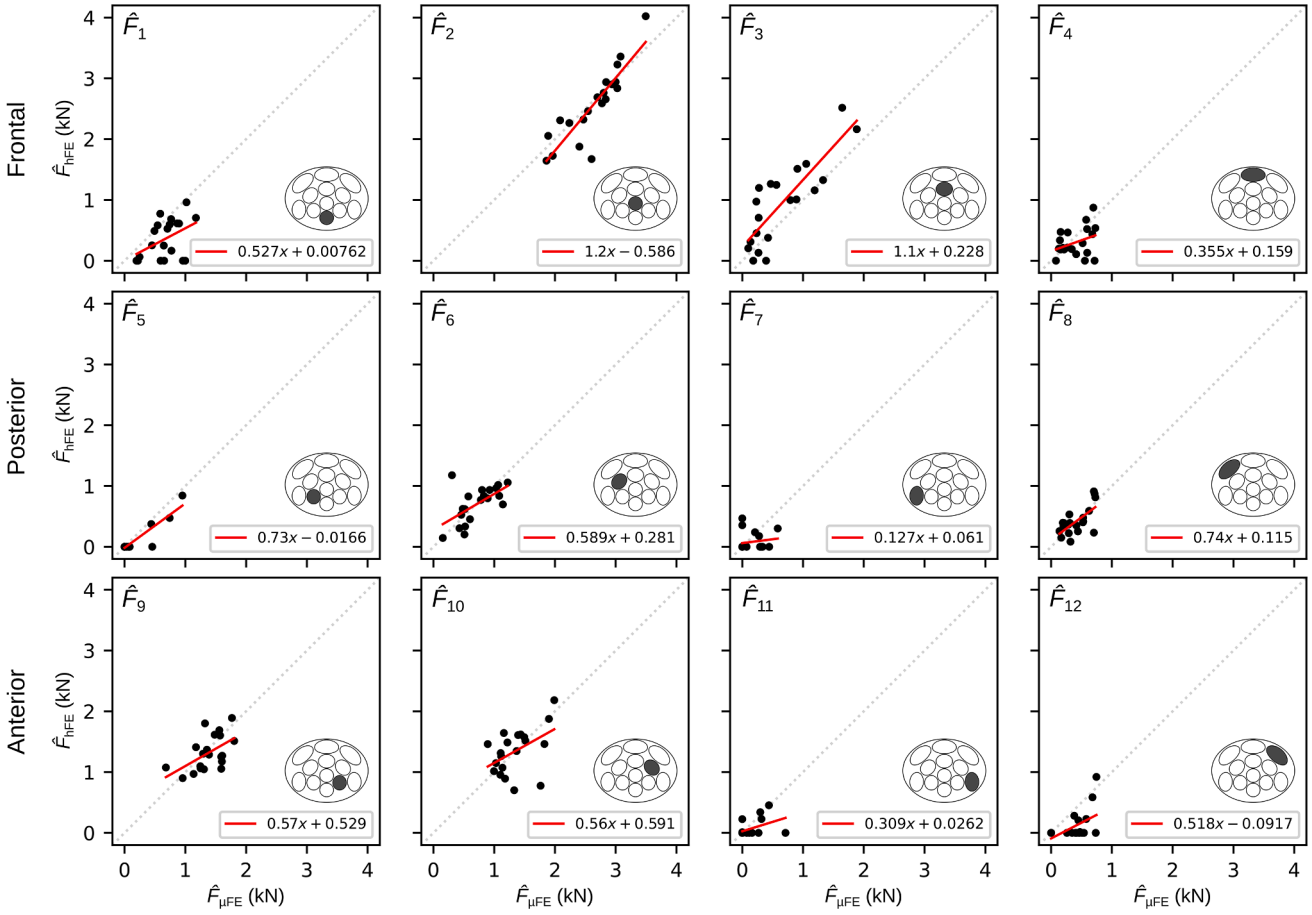

Fig. 8. Correlation of the calibrated load cases.

BV/TV over larger regions in the currently used hFE models. Artificial coarsening of the QCT images suggests that the results of IBR, especially the predicted peak force, are only slightly affected. Details on the artificial coarsening are given in the supplemental material.

The QCT and XCT2 scans were performed *ex vivo* and thus did not contain soft tissues. Soft tissue may also influence the scan quality, and the scans used here should be viewed as a best-case result. However, it should be mentioned that datasets containing both low-resolution *in vivo* and high-resolution scans are very hard to obtain, as they cannot be performed *in vivo*. Thus, comparing low- and high-resolution-based IBR can, at the time being, only be performed using *ex vivo* data.

A limitation from a clinical point of view is the requirement for BMD-calibrated images to create the FE models. Adding a calibration phantom in the CT scan is not yet routine in clinical practice and thus hinders the application of IBR as a retrospective tool. However, even if no calibration phantom was used in the CT scan, phantomless or asynchronous calibration may be applied [55] for opportunistic screening or retrospective analysis.

The FE models used several simplifications. The applied cartilage layer used a linear elastic material with the same Poisson's ratio as bone. This simplification was adopted for the hFE models to ensure comparability with µFE [19], where only a single Poisson's ratio can be used for the entire mesh. The cartilage layer was initially required only for the proper load transfer in the µFE models [16,56] and may not be necessary

for hFE models *per se*, as the load can be applied in different ways [57]. However, it was kept for the hFE models to produce comparable results towards μFE, and these restrictions may be lifted in the future for hFE models. A sensitivity study on the cartilage layer thickness was performed for all hFE models to ensure that the cartilage layer does not influence the results. Only a marginal change in predicted loads was observed for different cartilage thicknesses. Details regarding the sensitivity study can be found in the supplemental material.

The applied boundary conditions for the unit load cases are simplified and only partially reflect the *in vivo* loading scenario at the hip [58]. However, a scan of the full articulation was not available to produce proper contact models.

Lastly, the here used peak load calibration was only performed on a small data set and would have to be established on a larger cohort and possibly also calculated separately for sex and age groups in the future.

This study also lays the foundation for new research. A load prediction with hFE-based IBR and the possibility for clinical QCT images could be used in many different clinical scenarios. One would be the opportunistic screening for pathological loading alterations at the joint level. With such an early detection tool, interventions could be initiated before osteoarthritis evolves, for example. Previous studies showed that μFE-based IBR can be applied to predict different habitual joint loadings between primate species at the third metacarpal [59] or different loadings of the femoral head between different species [45]. However, the sensitivity of hFE-based IBR to changes in habitual activity or pathological loading alteration has not been assessed yet.

So far, the application of IBR was limited to small bones, bone segments, or relatively simple joints, such as the hip, where unit loads can be applied easily, especially in the case of μFE. However, hFE-based IBR also allows for the application in large bones and other joints which involve more complex unit load cases (e.g. joint contact).

Finally, other imaging methods could be used to obtain the density distribution of the bone to avoid CT scanning. These are, for example, 2D to 3D reconstruction from bi-planar X-rays [22] or using magnetic resonance imaging (MRI) with specific bone sequences [60]. Applying these modalities within the IBR framework would require additional studies.

To conclude, the here developed workflow was successfully applied to clinically feasible QCT images. The hip joint load predicted by hFE-based IBR using such QCT images was compared to μFE-based IBR based on high-resolution CT images. The essential steps in the workflow were the calibration of BV/TV from BMD and an additional calibration step for the predicted peak load magnitude of IBR. Using the peak load calibration allows for patient-specific load prediction with a good correlation of the peak loads compared to μFE-based IBR. Using hFE-based inverse bone remodeling allows for fast prediction and is thus suitable for clinical applications.

Declaration of generative AI and AI-assisted technologies in the writing process

During the preparation of this work the authors used “Grammarly”, “DeepL”, and “ChatGPT” in order to check the text for grammar and spelling mistakes and improve reading fluency. After using this tool/service, the authors reviewed and edited the content as needed and take full responsibility for the content of the published article.

Ethics statement

Samples were collected for a previous study [1] at the anatomy institute of the Lübeck University in accordance with the German law (“Gesetz über das Leichen-, Bestattungs- und Friedhofswesen des Landes Schleswig-Holstein - Abschnitt II, §9 (Leichenöffnung, anatomisch)” from 04.02.2005). All subjects had given consent for the scientific use of their bodies. No additional scans or experiments were conducted on the specimens for this study.

References (for ethics)

1. Iori, G., Heyer, F., Kilappa, V., Wyers, C., Varga, P., Schneider, J., Gräsel, M., Wendlandt, R., Barkmann, R., Bergh, J.P. van den, Raum, K.: BMD-based assessment of local porosity in human femoral cortical bone. Bone. 114, 50–61 (2018). 10.1016/j.bone.2018.05.028.

CRediT authorship contribution statement

Sebastian Bachmann: Writing – original draft, Visualization, Validation, Software, Methodology, Formal analysis, Conceptualization. **Gianluca Iori:** Writing – review & editing, Data curation. **Kay Raum:** Writing – review & editing, Data curation. **Dieter H. Pahr:** Writing – review & editing, Validation, Supervision, Software, Methodology, Conceptualization. **Alexander Synek:** Writing – original draft, Validation, Supervision, Methodology, Formal analysis, Conceptualization.

Declaration of competing interest

The authors declare the following financial interests/personal relationships which may be considered as potential competing interests:

CEO of Dr. Pahr Ingenieurs e.U., which develops and distributes Medtool - DHP. If there are other authors, they declare that they have no known competing financial interests or personal relationships that could have appeared to influence the work reported in this paper.

Acknowledgments

QCT scans were performed at the University Hospital Schleswig-Holstein, Campus Kiel (Germany) by Reinhard Barkmann. The authors acknowledge TU Wien Bibliothek for financial support through its Open Access Funding Programme.

Supplementary materials

Supplementary material associated with this article can be found, in the online version, at doi:10.1016/j.cmpb.2025.108805.

References

[1] B.M. Willie, E.A. Zimmermann, I. Vitienes, R.P. Main, S.V. Komarova, Bone adaptation: safety factors and load predictability in shaping skeletal form, Bone 131 (2020), https://doi.org/10.1016/j.bone.2019.115114.
[2] F. Taddei, I. Palmadori, W.R. Taylor, M.O. Heller, B. Bordini, A. Toni, E. Schileo, European society of biomechanics S.M. Perren award 2014: safety factor of the proximal femur during gait: a population-based finite element study, J. Biomech. 47 (2014) 3433–3440, https://doi.org/10.1016/j.jbiomech.2014.08.030.
[3] A. Paz, J. Lavikainen, M.J. Turunen, J.J. García, R.K. Korhonen, M.E. Mononen, Knee-loading predictions with neural networks improve finite element modeling classifications of knee osteoarthritis: data from the osteoarthritis initiative, Ann. Biomed. Eng. 52 (2024) 2569–2583, https://doi.org/10.1007/s10439-024-03549-2.
[4] T.M. Griffin, F. Guilak, The role of mechanical loading in the onset and progression of osteoarthritis, Exerc. Sport Sci. Rev. 33 (2005) 195, https://doi.org/10.1097/00003677-200510000-00008.
[5] P. Pankaj, Patient-specific modelling of bone and bone-implant systems: the challenges, Int. J. Numer. Method. Biomed. Eng. 29 (2013) 233–249, https://doi.org/10.1002/cnm.2536.
[6] G. Bergmann, A. Bender, J. Dymke, G. Duda, P. Damm, Standardized loads acting in hip implants, PLoS One 11 (2016) e0155612, https://doi.org/10.1371/journal.pone.0155612.
[7] K. Song, A.E. Anderson, J.A. Weiss, M.D. Harris, Musculoskeletal models with generic and subject-specific geometry estimate different joint biomechanics in dysplastic hips, Comput. Methods Biomech. Biomed. Engin. 22 (2019) 259–270, https://doi.org/10.1080/10255842.2018.1550577.
[8] G. Lenaerts, W. Bartels, F. Gelaude, M. Mulier, A. Spaepen, G.V Perre, I. Jonkers, Subject-specific hip geometry and hip joint centre location affects calculated contact forces at the hip during gait, J. Biomech. 42 (2009) 1246–1251, https://doi.org/10.1016/j.jbiomech.2009.03.037.
[9] M. Tomasi, A. Artoni, L. Mattei, F. Di Puccio, On the estimation of hip joint loads through musculoskeletal modeling, Biomech. Model. Mechanobiol. 22 (2023) 379–400, https://doi.org/10.1007/s10237-022-01668-0.
[10] A.A. Zadpoor, H. Weinans, Patient-specific bone modeling and analysis: the role of integration and automation in clinical adoption, J. Biomech. 48 (2015) 750–760, https://doi.org/10.1016/j.jbiomech.2014.12.018.

[11] P. Pivonka, A. Park, M.R. Forwood, Functional adaptation of bone: the mechanostat and beyond. Multiscale Mechanobiology of Bone Remodeling and Adaptation, Springer International Publishing, 2017, pp. 1–60, https://doi.org/10.1007/978-3-319-58845-2_1.
[12] C. Ruff, B. Holt, E. Trinkaus, Who's afraid of the big bad Wolff?: "Wolff's law" and bone functional adaptation, Am. J. Phys. Anthropol. 129 (2006) 484–498, https://doi.org/10.1002/ajpa.20371.
[13] M.A. Bona, L.D. Martin, K.J. Fischer, A contact algorithm for density-based load estimation, J. Biomech. 39 (2006) 636–644, https://doi.org/10.1016/j.jbiomech.2005.01.006.
[14] K.J. Fischer, C.R. Jacobs, D.R. Carter, Computational method for determination of bone and joint loads using bone density distributions, J. Biomech. 28 (1995) 1127–1135, https://doi.org/10.1016/0021-9290(94)00182-4.
[15] P. Christen, B. Rietbergen, F.M. Lambers, R. Müller, K. Ito, Bone morphology allows estimation of loading history in a murine model of bone adaptation, Biomech. Model. Mechanobiol. 11 (2011) 483–492, https://doi.org/10.1007/s10237-011-0327-x.
[16] A. Synek, D.H. Pahr, Plausibility and parameter sensitivity of micro-finite element-based joint load prediction at the proximal femur, Biomech. Model. Mechanobiol. 17 (2017) 843–852, https://doi.org/10.1007/s10237-017-0996-1.
[17] M. Walle, F.C. Marques, N. Ohs, M. Blauth, R. Müller, C.J. Collins, Bone mechanoregulation allows subject-specific load estimation based on time-lapsed micro-CT and HR-pQCT *in vivo*, Front. Bioeng. Biotechnol. 9 (2021), https://doi.org/10.3389/fbioe.2021.677985.
[18] S. Bachmann, D.H. Pahr, A. Synek, A density-dependent target stimulus for inverse bone (*Re*)modeling with homogenized finite element models, Ann. Biomed. Eng. (2022), https://doi.org/10.1007/s10439-022-03104-x.
[19] S. Bachmann, D.H. Pahr, A. Synek, Hip joint load prediction using inverse bone remodeling with homogenized FE models: comparison to micro-FE and influence of material modeling strategy, Comput. Methods Programs Biomed. (2023) 107549, https://doi.org/10.1016/j.cmpb.2023.107549.
[20] D. Schenk, P. Zysset, Personalized loading conditions for homogenized finite element analysis of the distal sections of the radius, Biomech. Model. Mechanobiol. (2022), https://doi.org/10.1007/s10237-022-01656-4.
[21] P. Zysset, D. Pahr, K. Engelke, H.K. Genant, M.R. McClung, D.L. Kendler, C. Recknor, M. Kinzl, J. Schwiedrzik, O. Museyko, A. Wang, C. Libanati, Comparison of proximal femur and vertebral body strength improvements in the FREEDOM trial using an alternative finite element methodology, Bone 81 (2015) 122–130, https://doi.org/10.1016/j.bone.2015.06.025.
[22] L. Steiner, A. Synek, D.H. Pahr, Femoral strength can be predicted from 2D projections using a 3D statistical deformation and texture model with finite element analysis, Med. Eng. Phys. 93 (2021) 72–82, https://doi.org/10.1016/j.medengphy.2021.05.012.
[23] L. Steiner, A. Synek, D.H. Pahr, Femoral bone strength prediction using isotopological B-spline-transformed meshes, Biomechanics 2 (2022) 125–137, https://doi.org/10.3390/biomechanics2010012.
[24] G. Iori, F. Heyer, V. Kilappa, C. Wyers, P. Varga, J. Schneider, M. Gräsel, R. Wendlandt, R. Barkmann, J.P. Bergh, K. Raum, BMD-based assessment of local porosity in human femoral cortical bone, Bone 114 (2018) 50–61, https://doi.org/10.1016/j.bone.2018.05.028.
[25] E. Dall'Ara, B. Luisier, R. Schmidt, M. Pretterklieber, F. Kainberger, P. Zysset, D. Pahr, DXA predictions of human femoral mechanical properties depend on the load configuration, Med. Eng. Phys. 35 (2013) 1564–1572, https://doi.org/10.1016/j.medengphy.2013.04.008.
[26] C. Graeff, F. Marin, H. Petto, O. Kayser, A. Reisinger, J. Peña, P. Zysset, C.C. Glüer, High resolution quantitative computed tomography-based assessment of trabecular microstructure and strength estimates by finite-element analysis of the spine, but not DXA, reflects vertebral fracture status in men with glucocorticoid-induced osteoporosis, Bone 52 (2013) 568–577, https://doi.org/10.1016/j.bone.2012.10.036.
[27] J.A. Peña, F. Thomsen, T. Damm, G.M. Campbell, J. Bastgen, R. Barkmann, C. C. Glüer, Bone-marrow densitometry: assessment of marrow space of human vertebrae by single energy high resolution-quantitative computed tomography, Med. Phys. 43 (2016) 4174–4183, https://doi.org/10.1118/1.4950874.
[28] A. Krebs, C. Graeff, I. Frieling, B. Kurz, W. Timm, K. Engelke, C.C. Glüer, High resolution computed tomography of the vertebrae yields accurate information on trabecular distances if processed by 3D fuzzy segmentation approaches, Bone 44 (2009) 145–152, https://doi.org/10.1016/j.bone.2008.08.131.
[29] C. Graeff, W. Timm, T.N. Nickelsen, J. Farrerons, F. Marín, C. Barker, C.C. Glüer, Monitoring teriparatide-associated changes in vertebral microstructure by high-resolution CT *In vivo*: results from the EUROFORS study*, J. Bone Miner. Res. 22 (2007) 1426–1433, https://doi.org/10.1359/jbmr.070603.
[30] P. Christen, F.A. Schulte, A. Zwahlen, B. Rietbergen, S. Boutroy, L.J. Melton, S. Amin, S. Khosla, J. Goldhahn, R. Müller, Voxel size dependency, reproducibility and sensitivity of an *in vivo* bone loading estimation algorithm, J. R. Soc. Interface 13 (2016) 20150991, https://doi.org/10.1098/rsif.2015.0991.
[31] B.C. Lowekamp, D.T. Chen, L. Ibáñez, D. Blezek, The design of simpleITK, Front. Neuroinform. 7 (2013), https://doi.org/10.3389/fninf.2013.00045.
[32] E. Dall'Ara, B. Luisier, R. Schmidt, F. Kainberger, P. Zysset, D. Pahr, A nonlinear QCT-based finite element model validation study for the human femur tested in two configurations *in vitro*, Bone 52 (2013) 27–38, https://doi.org/10.1016/j.bone.2012.09.006.
[33] D.H. Pahr, P.K. Zysset, From high-resolution CT data to finite element models: development of an integrated modular framework, Comput. Methods Biomech. Biomed. Eng. 12 (2009) 45–57, https://doi.org/10.1080/10255840802144105.
[34] The CGAL Project, CGAL User and Reference Manual, CGAL Editorial Board, 2024.
[35] C. Geuzaine, J.F. Remacle, Gmsh: a 3-D finite element mesh generator with built-in pre- and post-processing facilities, Int. J. Numer. Methods Eng. 79 (2009) 1309–1331, https://doi.org/10.1002/nme.2579.
[36] B. Luisier, E. Dall'Ara, D.H. Pahr, Orthotropic HR-pQCT-based FE models improve strength predictions for stance but not for side-way fall loading compared to isotropic QCT-based FE models of human femurs, J. Mech. Behav. Biomed. Mater. 32 (2014) 287–299, https://doi.org/10.1016/j.jmbbm.2014.01.006.
[37] D.H. Pahr, P.K. Zysset, A comparison of enhanced continuum FE with micro FE models of human vertebral bodies, J. Biomech. 42 (2009) 455–462, https://doi.org/10.1016/j.jbiomech.2008.11.028.
[38] T. Gross, D.H. Pahr, P.K. Zysset, Morphology–elasticity relationships using decreasing fabric information of human trabecular bone from three major anatomical locations, Biomech. Model. Mechanobiol. 12 (2012) 793–800, https://doi.org/10.1007/s10237-012-0443-2.
[39] J. Panyasantisuk, D.H. Pahr, T. Gross, P.K. Zysset, Comparison of mixed and kinematic uniform boundary conditions in homogenized elasticity of femoral trabecular bone using microfinite element analyses, J. Biomech. Eng. 137 (2015), https://doi.org/10.1115/1.4028968.
[40] H.S. Hosseini, A. Dünki, J. Fabech, M. Stauber, N. Vilayphiou, D. Pahr, M. Pretterklieber, J. Wandel, B. Rietbergen, P.K. Zysset, Fast estimation of Colles' fracture load of the distal section of the radius by homogenized finite element analysis based on HR-pQCT, Bone 97 (2017) 65–75, https://doi.org/10.1016/j.bone.2017.01.003.
[41] D. Schenk, M. Indermaur, M. Simon, B. Voumard, P. Varga, M. Pretterklieber, K. Lippuner, P. Zysset, Unified validation of a refined second-generation HR-pQCT based homogenized finite element method to predict strength of the distal segments in radius and tibia, J. Mech. Behav. Biomed. Mater. 131 (2022) 105235, https://doi.org/10.1016/j.jmbbm.2022.105235.
[42] T.P. Harrigan, M. Jasty, R.W. Mann, W.H. Harris, Limitations of the continuum assumption in cancellous bone, J. Biomech. 21 (1988) 269–275, https://doi.org/10.1016/0021-9290(88)90257-6.
[43] P.K. Zysset, A. Curnier, An alternative model for anisotropic elasticity based on fabric tensors, Mech. Mater. 21 (1995) 243–250, https://doi.org/10.1016/0167-6636(95)00018-6.
[44] C. Flaig, P. Arbenz, A scalable memory efficient multigrid solver for micro-finite element analyses based on CT images, Parallel Comput. 37 (2011) 846–854, https://doi.org/10.1016/j.parco.2011.08.001.
[45] P. Christen, K. Ito, F. Galis, B. Rietbergen, Determination of hip-joint loading patterns of living and extinct mammals using an inverse Wolff's law approach, Biomech. Model. Mechanobiol. 14 (2014) 427–432, https://doi.org/10.1007/s10237-014-0602-8.
[46] P. Virtanen, R. Gommers, T.E. Oliphant, M. Haberland, T. Reddy, D. Cournapeau, E. Burovski, P. Peterson, W. Weckesser, J. Bright, S.J. Walt, M. Brett, J. Wilson, K. J. Millman, N. Mayorov, A.R.J. Nelson, E. Jones, R. Kern, E. Larson, C.J. Carey, İ. Polat, Y. Feng, E.W. Moore, J. VanderPlas, D. Laxalde, J. Perktold, R. Cimrman, I. Henriksen, E.A. Quintero, C.R. Harris, A.M. Archibald, A.H. Ribeiro, F. Pedregosa, Mulbregt, P. van, S.1. Contributors, SciPy 1.0: fundamental algorithms for scientific computing in python, Nat. Methods 17 (2020) 261–272, https://doi.org/10.1038/s41592-019-0686-2.
[47] E. Verhulp, B. Rietbergen, R. Huiskes, Comparison of micro-level and continuum-level voxel models of the proximal femur, J. Biomech. 39 (2006) 2951–2957, https://doi.org/10.1016/j.jbiomech.2005.10.027.
[48] R.A. Pearson, G.M. Treece, Measurement of the bone endocortical region using clinical CT, Med. Image Anal. 44 (2018) 28–40, https://doi.org/10.1016/j.media.2017.11.006.
[49] T.D. Brown, D.T. Shaw, *In vitro* contact stress distributions in the natural human hip, J. Biomech. 16 (1983) 373–384, https://doi.org/10.1016/0021-9290(83)90071-4.
[50] M. Wurm, A universal and fast method to solve linear systems with correlated coefficients using weighted total least squares, Meas. Sci. Technol. 33 (2021) 015017, https://doi.org/10.1088/1361-6501/ac32ec.
[51] P. Christen, K. Ito, A.A. Santos, R. Müller, B. Rietbergen, Validation of a bone loading estimation algorithm for patient-specific bone remodelling simulations, J. Biomech. 46 (2013) 941–948, https://doi.org/10.1016/j.jbiomech.2012.12.012.
[52] M.J. Willemink, M. Persson, A. Pourmorteza, N.J. Pelc, D. Fleischmann, Photon-counting CT: technical principles and clinical prospects, Radiology 289 (2018) 293–312, https://doi.org/10.1148/radiol.2018172656.
[53] C.H. McCollough, K. Rajendran, F.I. Baffour, F.E. Diehn, A. Ferrero, K. N. Glazebrook, K.K. Horst, T.F. Johnson, S. Leng, A. Mileto, P.S. Rajiah, B. Schmidt, L. Yu, T.G. Flohr, J.G. Fletcher, Clinical applications of photon counting detector CT, Eur. Radiol. 33 (2023) 5309–5320, https://doi.org/10.1007/s00330-023-09596-y.
[54] S.J.O. Rytky, A. Tiulpin, M.A.J. Finnilä, S.S. Karhula, A. Sipola, V. Kurttila, M. Valkealahti, P. Lehenkari, A. Joukainen, H. Kröger, R.K. Korhonen, S. Saarakkala, J. Niinimäki, Clinical super-resolution computed tomography of bone microstructure: application in musculoskeletal and dental imaging, Ann. Biomed. Eng. 52 (2024) 1255–1269, https://doi.org/10.1007/s10439-024-03450-y.
[55] C.A. Mallio, D. Vertulli, C. Bernetti, M. Stiffi, F. Greco, J. Van Goethem, P. M. Parizel, C.C. Quattrocchi, B. Beomonte Zobel, Phantomless computed tomography-based quantitative bone mineral density assessment: a literature review, Appl. Sci. 14 (2024) 1447, https://doi.org/10.3390/app14041447.
[56] P. Christen, K. Ito, I. Knippels, R. Müller, G.H. Lenthe, B. Rietbergen, Subject-specific bone loading estimation in the human distal radius, J. Biomech. 46 (2013) 759–766, https://doi.org/10.1016/j.jbiomech.2012.11.016.

[57] A.Y. Bavil, E. Eghan-Acquah, L.E. Diamond, R. Barrett, C.P. Carty, M. Barzan, A. Nasseri, D.G. Lloyd, D.J. Saxby, S. Feih, Effect of different constraining boundary conditions on simulated femoral stresses and strains during gait, Sci. Rep. 14 (2024) 10808, https://doi.org/10.1038/s41598-024-61305-x.

[58] P. Yang, T.Y. Lin, J.L. Xu, H.Y. Zeng, D. Chen, B.L. Xiong, F.X. Pang, Z.Q. Chen, W. He, Q.S. Wei, Q.W. Zhang, Finite element modeling of proximal femur with quantifiable weight-bearing area in standing position, J. Orthop. Surg. Res. 15 (2020) 384, https://doi.org/10.1186/s13018-020-01927-9.

[59] A. Synek, C.J. Dunmore, T.L. Kivell, M.M. Skinner, D.H. Pahr, Inverse remodelling algorithm identifies habitual manual activities of primates based on metacarpal bone architecture, Biomech. Model. Mechanobiol. 18 (2018) 399–410, https://doi.org/10.1007/s10237-018-1091-y.

[60] S. Jerban, S. Alenezi, A.M. Afsahi, Y. Ma, J. Du, C.B. Chung, E.Y. Chang, MRI-based mechanical competence assessment of bone using micro finite element analysis (micro-FEA): review, Magn. Reson. Imaging 88 (2022) 9–19, https://doi.org/10.1016/j.mri.2022.01.009.